Progress in Natural Science: Materials International 36 (2026) 102–109

HOSTED BY

Contents lists available at ScienceDirect

Progress in Natural Science: Materials International

journal homepage: www.elsevier.com/locate/pnsmi

Nanocrystalline-glass heterostructure via phase engineering for efficient hydrogen evolution

Huahai Chang[a], Yiyuan Yang[a,b], Fan Yu[a], Shunda Jiang[a], Xueqian Wang[a], Zhe Jia[a,*], Baolong Shen[a,**]

[a] School of Materials Science and Engineering, Jiangsu Key Laboratory for Advanced Metallic Materials, Southeast University, Nanjing, 211189, China
[b] Hong Kong Branch of National Precious Metals Material Engineering Research Center and Department of Mechanical Engineering, City University of Hong Kong, Hong Kong SAR, China

ARTICLE INFO

Keywords:
Multi-principal element alloys
Phase engineering
Dealloying
Heterostructure
Water electrolysis

ABSTRACT

The development of efficient, stable, and low-cost electrocatalysts is crucial for hydrogen production via water electrolysis. While multi-principal element alloys (MPEAs) show great potential due to their multi-component synergy and tunable electronic structures, their practical application is often hampered by insufficient active sites and poor long-term stability. Herein, we report a phase-engineering-guided dealloying strategy to fabricate a high-performance MPEA catalyst for hydrogen evolution reaction (HER). This approach employs a triple-phase $Al_{60}Ni_{27}Fe_5Co_5Mo_3$ precursor, wherein chemical dealloying in an alkaline medium transforms the BCC parent phase into an ordered B2 phase, while completely dissolving the less stable FCC and tetragonal phases. This process results in a unique heterogeneous structure of Ni-based oxide nanocrystals enveloped by a Mo-rich metallic glass phase, coating the B2 phase surface. Benefiting from the abundant heterogeneous interfaces and synergistic interactions among multiple phases generated during dealloying, the catalyst exhibits outstanding activity and stability for HER in alkaline media, achieving a low overpotential of 35 mV at 10 mA cm^{-2} and exceptional durability for 500 h at 100 mA cm^{-2} with negligible activity degradation. This work presents a novel pathway for designing multiphase MPEAs and underscores the significant potential of high-performance electrocatalyst preparation by combining phase engineering with dealloying.

1. Introduction

The large-scale production of clean hydrogen is essential for establishing a sustainable energy system [1,2]. Electrocatalytic water splitting powered by renewable energy has been recognized as a key pathway for producing green hydrogen, owing to its environmental benefits and the high purity of the outcome [3,4]. However, the development of electrocatalysts that offer high activity, excellent stability, and low cost to meet the demands of industrial applications remains a significant challenge [5,6]. Significant potential has been demonstrated by high-performance catalysts such as metal-organic frameworks [7–9], single-atom materials [10,11], layered double hydroxides [12,13], and transition metal compounds [14–16] in recent years. The poor long-term stability of these materials, primarily due to structural collapse and the deactivation of active sites, limits their ability to meet the durability demands of practical industrial applications, despite their excellent catalytic activity and selectivity [17]. The current situation has prompted ongoing exploration of new catalyst systems by researchers, alongside efforts to establish design principles for their activation and stabilization.

Multi-principal element alloys (MPEAs), generally including medium-entropy alloys (MEAs) and high-entropy alloys (HEAs) characterized by their unique compositional flexibility and structural features, have emerged as a key focus in water electrolysis research [18–22], and promising candidates have been reported including high-entropy oxides [23,24], sulfides [25], phosphide [26], intermetallics [27,28], and even metallic glasses [29–31], bringing fresh momentum to catalyst design. Significant multicomponent synergistic effects arise from their complex chemical environments, and their tunable electronic structures hold promise for overcoming the limitations associated with adsorption energy control [32–34]. However, most current MPEA catalysts are still centered on thermodynamically stable

* Corresponding author.
** Corresponding author.
E-mail addresses: zhejia@seu.edu.cn (Z. Jia), blshen@seu.edu.cn (B. Shen).

https://doi.org/10.1016/j.pnsc.2025.12.001
Received 10 November 2025; Received in revised form 3 December 2025; Accepted 6 December 2025
Available online 18 December 2025

single-phase or dual-phase solid solution structures [35–37], the structural simplicity significantly restricts the diversity of active sites and hinders the full exploitation of interfacial synergistic effects. Thus, designing multiphase precursors and utilizing selective corrosion to create abundant heterogeneous structures and phase interfaces, offers a promising pathway to overcome current performance bottlenecks in MPEA catalytic materials.

Phase engineering has emerged as a powerful approach to modulate the electronic structure and reaction pathways of electrocatalysts by constructing multiphase heterogeneous architectures [38–42]. Coupled with dealloying techniques, it enables nanoscale control over phase composition and interface formation. In multiphase MPEAs, electrochemical selective etching leverages differences in phase stability to create porous structures with abundant heterogeneous interfaces. These structural features tailor the local coordination environment of active sites and adjust *d*-band center, thereby optimizing the adsorption/desorption behavior of reaction intermediates. This strategy shows broad potential in electrocatalytic applications, including water splitting [43, 44], oxygen reduction [45], CO_2 reduction [46] and nitrate reduction reaction [47–49]. Hence, the integration of phase engineering and dealloying offers a promising route for designing efficient and durable electrocatalytic systems.

Here, a phase-engineering-guided multiphase precursor dealloying strategy was developed for the fabrication of high-performance hydrogen evolution electrocatalysts. $Al_{60}Ni_{27}Fe_5Co_5Mo_3$ powders with a thriple-phase structure comprising body-centered cubic (BCC), face-centered cubic (FCC), and tetragonal phases were synthesized via gas atomization (GAM) technology and employed as the precursor. Subsequent chemical dealloying in an alkaline solution enabled the selective removal of the FCC and tetragonal phases, while the BCC parent phase was converted into an ordered B2 framework. This process simultaneously induced the in-situ precipitation of Ni-based oxide nanocrystals and the formation of a Mo-rich amorphous phase, resulting in the construction of a catalyst featuring an amorphous/nanocrystalline heterogeneous structure. Owing to the synergistic interactions among multiple phases and the abundant heterogeneous interfaces generated during dealloying, the catalyst demonstrated outstanding catalytic activity and stability for hydrogen evolution reaction (HER) in alkaline media, the dealloyed powder catalysts achieved overpotentials of 35 mV at a current density of 10 mA cm^{-2} for HER under alkaline conditions, maintaining stability for 500 h at a current density of 100 mA cm^{-2} with negligible activity degradation. A new approach for designing multiphase MPEA catalysts has been presented in this study, which also provides valuable insights for material design strategies that integrate phase engineering with dealloying techniques.

2. Materials and methods

2.1. Materials

Fe (99.99 wt%), Co (99.99 wt%), Ni (99.99 wt%), Mo (99.99 wt%), and Al (99.99 wt%) granules were weighed and mixed to give a theoretical atomic composition of $Fe_5Co_5Ni_{30}Al_{60}$ and $Fe_5Co_5Ni_{27}Mo_3Al_{60}$. Analytical grade potassium hydroxide (KOH) and absolute ethanol were supplied by Aladdin (Shanghai, China) and Nanjing WANQING Chemical Glassware & Instrument Co., Ltd (Nanjing, China). Deionized water was used to dilute the KOH solutions. Raney nickel was supplied by Macklin (Shanghai, China).

2.2. Materials preparation

The MPEA powders were prepared by arc-melting and gas atomization method. Specifically, a master alloy ingot (~20 g) with an atomic composition of $Al_{60}Fe_5Co_5Ni_{30-x}Mo_x$ (X = 0, 3) was initially prepared by arc-melting under high-purity argon (Ar) atmosphere with Ti-gettering to minimize oxidation. The ingot was remelted at least four times to ensure the homogeneity of metal elements. Afterwards, the master alloy ingot was cut into pieces that were remelted in a quartz crucible. Subsequently the melt was atomized by a jet of nitrogen at a gas pressure of 8 MPa. The whole process was under Ar atmosphere. The atomized molten metal transformed into powders, and the rapidly cooled powders were passed through a sieve (<38 μm) into the powder collector. With regard to the chemical dealloying process, the raw powders were treated in a 3.0 M KOH solution for 2 h until bubble evolution ceased. The dealloyed powders were then washed by deionized water and ethanol three times, respectively. To test the HER performance of MPEAs, the dealloyed powders were dispersed into inks and were loaded on a bare Nickel foam (NF). And then NF was cut into rectangular dimensions of 5 mm × 8 mm × 0.5 mm as the working electrode.

2.3. Materials characterization

Phase structures were identified by X-ray diffraction (XRD, Bruker D8 Discover) using Cu-Kα radiation with a step size of 0.02° and a scan rate of 0.15 s per step. Surface morphology and elemental distribution were examined by scanning electron microscopy (SEM, Zeiss Ultra Plus) equipped with energy-dispersive X-ray spectroscopy (EDS). Microstructural analysis was performed using high-resolution transmission electron microscopy (HRTEM, Talos F200X) coupled with selected-area electron diffraction (SAED) and EDS. Atomic-resolution scanning transmission electron microscopy (STEM) and EDS mapping were conducted on an aberration-corrected transmission electron microscopy (AC-TEM, FEI Themis Z). Specimens for TEM analysis were prepared by focused ion beam (FIB) milling. Surface chemistry was analyzed by X-ray photoelectron spectroscopy (XPS, Thermo Scientific K-Alpha). Inductively coupled plasma optical emission spectrometry (ICP-OES) was used to quantify metal ion dissolution after stability tests.

2.4. Electrochemical measurements

Electrocatalytic performances were evaluated in a standard three-electrode system using a CHI760E electrochemical workstation. A graphite rod and a Hg/HgO electrode were used as the counter and reference electrodes, respectively. The working electrode was prepared by loading 20 μL catalyst ink onto bare NF (0.4 cm^2) with mass loading of 1.5 mg cm^{-2}. The catalyst ink was formulated by dispersing 30 mg dealloyed MPEA powders in a mixture of 950 μL ethanol and 50 μL Nafion solution. For comparison, commercial Raney nickel catalyst was also tested under identical conditions. All potentials were calibrated to the reversible hydrogen electrode (RHE) scale using the equation: $E_{RHE} = E_{Hg/HgO} + 0.0591 \times pH + 0.098$. Prior to measurement, cyclic voltammetry (CV) was conducted for 50 cycles at 100 mV s^{-1} to stabilize the electrode. Linear sweep voltammetry (LSV) was performed at a scan rate of 5 mV s^{-1} with *iR* compensation. Electrochemical impedance spectroscopy (EIS) was carried out in the frequency range of 10^{-1}- 10^5 Hz. The electrochemical active surface area (ECSA) was estimated from the double-layer capacitance (C_{dl}) determined by CV measurements at various scan rates (10–50 mV s^{-1}) in the non-faradaic region (ECSA = C_{dl}/C_s, where C_s is the specific capacitance per unit area. In this work, C_s was chosen as 0.04 mF cm^{-2} in 1.0 M KOH). Durability tests were conducted by chronoamperometry at a constant current density of 100 mA cm^{-2} without *iR*. In situ Raman spectra were acquired using a confocal microscope (WiTec Alpha300) with a 532 nm laser source. A homemade Raman cell was used to conduct the in situ electrochemical Raman experiments.

3. Results

3.1. Preparation and characterization of MPEA powders

MPEA powders with different molybdenum contents were all prepared using the GAM (Fig. 1a). We named the powders with

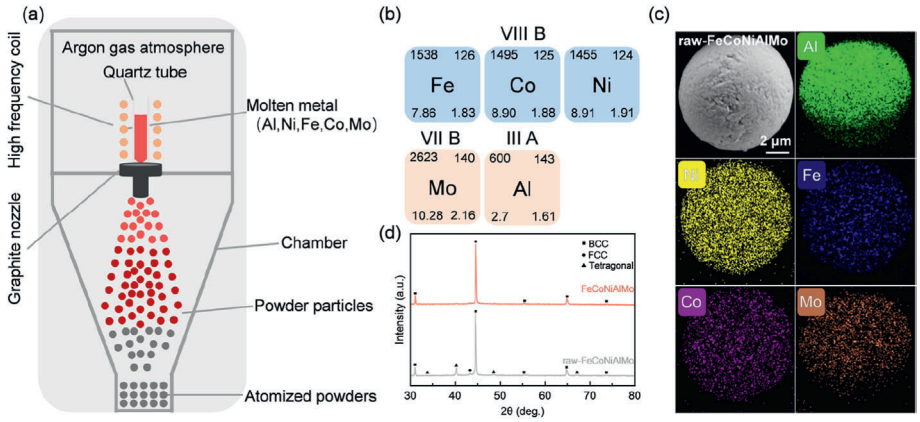

Fig. 1. Preparation and characterization of MPEA powders. (a) Schematic illustration of the preparation of $Al_{60}Fe_5Co_5Ni_{30-X}Mo_X$ MPEA powders by gas atomization method. (b) Schematic diagram of element selection. (c) SEM images with EDS mapping of raw-FeCoNiAlMo. (d) XRD patterns of FeCoNiAlMo before and after dealloying.

molybdenum contents of 0, 3 as raw FeCoNiAl and raw FeCoNiAlMo, respectively. Following repeated melting cycles to ensure homogeneity, the molten alloy was held in a quartz crucible to maintain its liquid state. It was then directed through a nozzle into the atomization chamber, where it was disintegrated into fine droplets by a high-velocity nitrogen gas stream and rapidly solidified. The resulting spherical powder was finally collected in a dedicated container. The elemental composition was meticulously engineered to fulfill specific and complementary roles during the dealloying process and in the final catalytic architecture. In Fig. 1b, Al serves as a sacrificial element to create a porous skeleton through selective etching [50]. Ni constitutes the primary catalytic phase for the HER [51]. Fe and Co are incorporated to modulate the electronic structure of Ni active sites, optimizing the adsorption free energy of reactive intermediates [52]. Mo acts as a critical amorphization promoter and stabilizer, forming a distinct amorphous phase while may additionally fine-tuning hydrogen adsorption energy [53]. The deliberate multi-functional integration of these elements aiming to result in a synergistic enhancement, yielding an electrocatalyst with high density of active sites, and superior HER activity and durability. Fig. 1c and Fig. S1 show the SEM with EDS images of the raw FeCoNiAlMo powder (denoted as raw-FeCoNiAlMo hereafter) and the dealloyed FeCoNiAlMo powder (denoted as FeCoNiAlMo hereafter), showing uniformly spherical particles with homogeneous elemental distribution. Similarly, the raw FeCoNiAl powder (denoted as raw-FeCoNiAl hereafter) and the dealloyed FeCoNiAl powder (denoted as FeCoNiAl hereafter) exhibit uniform spherical morphology and uniformly distributed elements (Fig. S2), demonstrating the reliability of the GAM. Interestingly, the rapid cooling of molten metal into particles under the impact of a high-velocity air stream resulted in surface rupture due to the mutual effects. The XRD results indicated that raw-FeCoNiAlMo possessed a tri-phase structure consisting of a BCC phase, a FCC phase and a tetragonal phase (Fig. 1d).

To further confirm the tri-phase structure of raw-FeCoNiAlMo, HAADF-STEM characterization and the corresponding EDS mapping

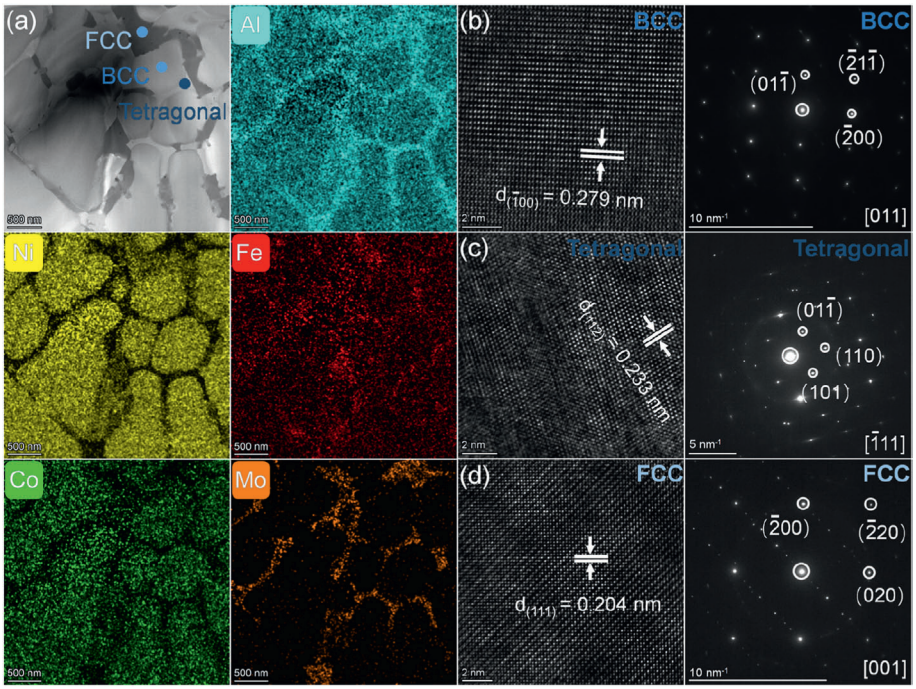

Fig. 2. Microstructural characterization of raw-FeCoNiAlMo. (a) HAADF-STEM image and the corresponding EDS mapping. HRTEM image with the corresponding SAED patterns of (b) BCC, (c) tetragonal, and (d) FCC phases.

are shown in Fig. 2a, where the BCC, FCC and tetragonal phases were clearly distinguished based on different contrast. The BCC phase was identified by the SAED pattern along the zone axis of [011] (Fig. 2b) and $[\bar{1}11]$ (Fig. S3a), and the measured lattice spacing of 0.279 nm for $\{\bar{1}00\}$ plane is shown in Fig. 2b. The tetragonal phase was also identified by the SAED pattern along the zone axis of $[\bar{1}11]$ (Fig. 2c) and $[02\bar{1}]$ (Fig. S3b), and the measured lattice spacing of 0.233 nm for the {112} plane is shown in Fig. 2c. The FCC phase was also identified by the SAED pattern along the zone axis of [001] (Fig. 2d) and $[\bar{1}11]$ (Fig. S3c), and the *d*-spacings of 0.204 nm was determined for their {111} planes in Fig. 2d. The specific atomic compositions of the BCC, FCC and tetragonal phases were measured by EDS (Table S1). The atomic contents of Al (65.19 %) and Mo (18.06 %) in the tetragonal phase were higher than in the BCC (Al: 40.32 %, Mo: 1.41 %) and FCC (Al: 49.87 %, Mo: 0.07 %) phases, the contents of Co and Ni in the BCC phase (Co: 4.89 %, Ni: 39.63 %) were higher than in the FCC (Co: 4.22 %, Ni: 21.79 %) and tetragonal (Co: 1.49 %, Ni: 4.14 %) phases, whereas the contents of Fe in the BCC phase (Fe: 4.75 %) was lower than in the FCC (Fe: 12.54 %) and tetragonal (Fe: 7.25 %) phases. These results indicate that raw-FeCoNiAlMo contained tri-phase that are distinct both in crystalline structure and atomic composition.

In terms of structural evolution, XRD shows that the peaks of the tetragonal phase and the FCC phase gradually weakened with dealloying until disappeared (Fig. 1d), indicating that the tetragonal and FCC phases (with high content of Al) was relatively unstable in alkali. FCC and tetragonal phases were preferentially dealloyed at phase boundaries, evolving into a nanocrystalline-glass structure and the BCC phase was still observed (Fig. 3a). Fig. 3b and c show the HRTEM images with corresponding SAED patterns of the BCC phase. The SAED pattern presented superlattice spots of $\{\bar{1}00\}$, and the *d*-spacings of 0.288 nm was determined for their $\{\bar{1}00\}$ planes, which indicated that the original BCC phase had transformed into a B2 structure [54] after 2 h dealloying process with clear Bragg diffraction spots of $\{01\bar{1}\}$, $\{\bar{2}00\}$, and superlattice diffraction spots. Fig. 3d–f shows the HRTEM images with corresponding SAED patterns of the nanocrystalline-glass phase, many nanocrystals (yellow areas) are encapsulated by a metallic glass phase (white areas) creating abundant heterostructure interfaces. The exposed surface of these nanocrystals is predominantly the indexed {200} planes with interplanar spacing of 0.204 nm (Fig. 3e). The crystal structure of the nanocrystals was identified by SAED, confirming the presence of Ni-based oxide [55] with FCC structure. Figs. S4 and 5 and Table S1 show the elemental distribution and composition of the nanocrystalline-glass and B2 phases in the dealloyed FeCoNiAlMo powder. Ni, Fe, Co and O were relatively concentrated in the nanocrystalline phase, Mo was predominantly enriched in the metallic glass phase, with a much higher content than in the nanocrystalline phase and B2 phase. Ni and Al were highly ordered distributed in the B2 phase. AC-TEM image shows that Al occupy the vertex positions while Ni reside at the body-centered sites, and a small amount of Fe and Co was substituted at the Ni sites due to their similar properties. These findings indicated that nanocrystalline-glass phase mostly consisted of the Ni-based oxide specie with an FCC structure, and the B2 phase was an ordered multi-elemental intermetallic.

The evolution of chemical valence states of the raw FeCoNiAlMo powder surface and the dealloyed FeCoNiAlMo powder surface were examined by XPS (Fig. 4). The XPS spectra of the raw powder indicated the existence of Fe^0, Co^0, Ni^0, Mo^0, and Al^0 species on the surface. An O element signal was attributed to the inevitable surface oxidation during the sample preparation. The changes of the peak positions of all the components are summarized in Tables S2 and S3. The peaks for raw-FeCoNiAlMo included the Fe 2p peaks at 706.1 (Fe^0),709.7 (Fe^{2+}) and 712.3 (Fe^{3+}) eV, Co 2p peaks at 777.4 (Co^0) eV, Ni 2p peak at 852.6 (Ni^0) and 856.4 (Ni^{2+}) eV, Mo 3d peaks at 226.8 (Mo^0) eV, Al 2p peaks at 72.0 (Al^0) and 74.6 (Al^{3+}) eV, and O 1s peaks at 531.4 (M − OH) and 532.6 (adsorbed-O) eV.

With increasing dealloying time up to 2 h, the zero-valent Fe, Co, Ni, Al and Mo of the dealloyed powder surface evolved to higher valence states, suggesting that these metallic elements were oxidized and hydroxylated in the alkaline environment, which agrees with the concentration increase of metal hydroxides (M − OH) in the O 1s spectra. In the O 1s spectra, the two dominant spin-orbit peaks located at 531.5 and 532.5 eV corresponded to the metal hydroxides (M − OH) and adsorbed H_2O at oxygen vacancies, respectively [56]. Simultaneously, a negative shift in the O 1s binding energy was simultaneously observed, implying enhanced electron transfer to oxygen species. The strong electronic coupling between different elements suggests that their coexistence synergistically induces local charge redistribution. This electronic structure modulation effectively tailors the active sites, which is anticipated to contribute to the improved catalytic performance.

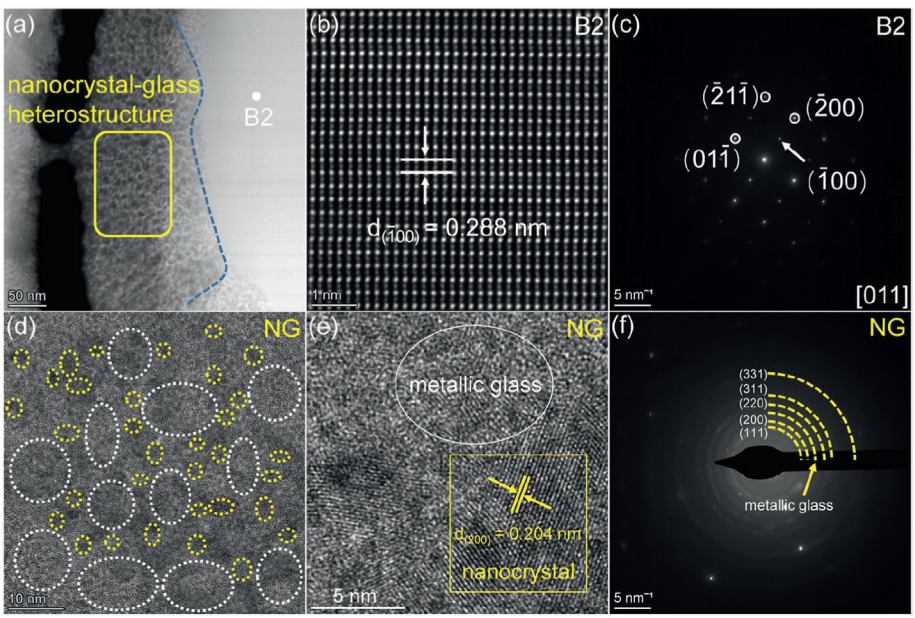

Fig. 3. Microstructural characterization of the dealloyed FeCoNiAlMo powder. (a) HAADF-STEM image. (b) AC-TEM image and (c) SAED patterns showing the formation of B2 phase. (d–e) HRTEM images and (f) SAED patterns showing the formation of nanocrystalline-glass structure.

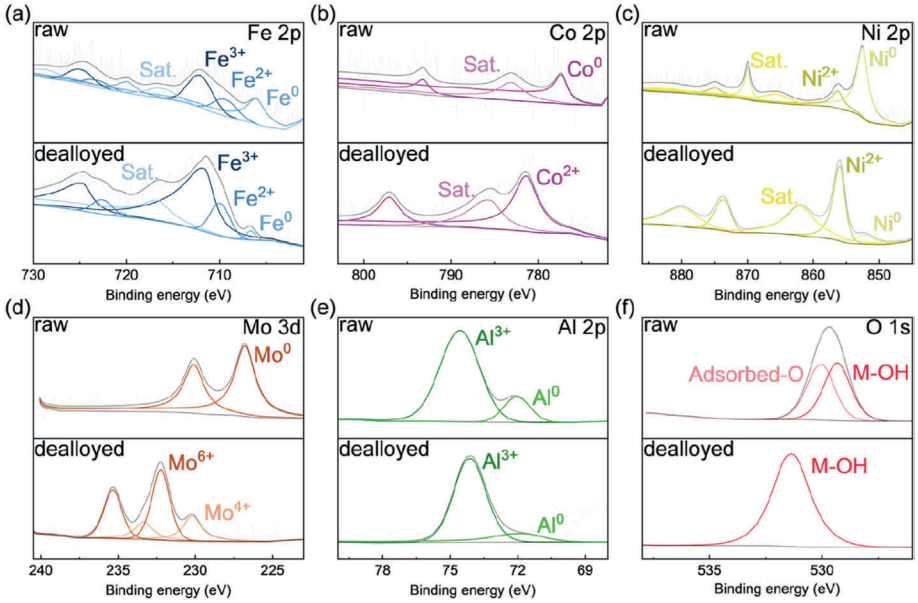

Fig. 4. High-resolution XPS results of FeCoNiAlMo powder before and after dealloying.

3.2. Electrochemical analysis

FeCoNiAlMo were directly used as working electrodes for investigating electrochemical water splitting performance in 1.0 M KOH solution. Commercial Raney nickel and FeCoNiAl were used to perform a comparative analysis. The potentials obtained in this work were 95 % *iR*-corrected to remove the ohmic drop across the electrolyte, unless specified otherwise. As shown in Fig. 5a, the FeCoNiAlMo catalyst exhibited the lowest overpotentials of 35 mV for the HER at a current density of 10 mA cm^{-2}, respectively, which were considerably lower than those of FeCoNiAl (176 mV for HER), the commercial metal catalysts (Raney nickel: 100 mV for HER) and bare NF (245 mV for HER). As shown in Fig. 5b, the Tafel slope of the FeCoNiAlMo catalyst was 57 mV dec^{-1}, which was the lowest value among FeCoNiAl (139 mV dec^{-1}), Raney nickel (77 mV dec^{-1}) and bare NF (100 mV dec^{-1}), implying fast reaction kinetics based on the Volmer-Heyrovsky mechanism [57]. To highlight the outstanding performance of the proposed FeCoNiAlMo catalyst, several state-of-the-art electrocatalysts for the HER were selected for performance comparison. The FeCoNiAlMo catalyst with nanocrystalline-glass structure has lower overpotentials than other

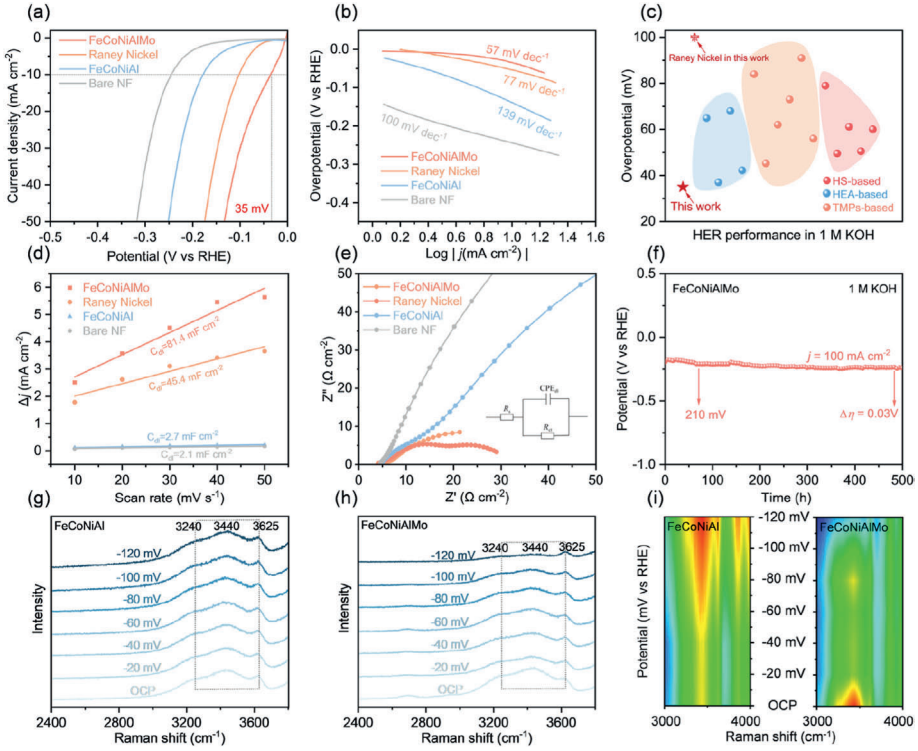

Fig. 5. Electrocatalytic performance of the MPEA powders for HER in 1.0 M KOH solution. Polarization curves of (a) HER at a scan rate of 5 mV s^{-1} with 95 % *iR* loss correction. (b) Tafel slopes for HER. (c) Comparison of overpotentials of various HER electrocatalysts at the current density of 10 mA cm^{-2} in 1.0 M KOH. (d) Double layer capacitances values. (e) Electrochemical impedance spectra curves. (f) HER stability performance of the FeCoNiAlMo catalyst at current density of 100 mA cm^{-2}. The operando Raman spectra of (g) FeCoNiAl, (h) FeCoNiAlMo in 1.0 M KOH solution in the range of 2400–3800 cm^{-1} at operating potentials from the OCP to - 120 mV (versus RHE). (i) Corresponding Raman contour map.

non-noble metal-based electrocatalysts, which included those of the heterostructure catalysts [58,59] high-entropy-alloy catalysts [60,61] and transition metal phosphide catalysts [62,63] in Fig. 5c and Table S4.

The ECSAs were evaluated via the C_{dl} obtained from CV curves at scanning rates of 10–50 mV s^{-1} (Fig. S6). As shown in Fig. 5d, the ECSA values of FeCoNiAlMo, FeCoNiAl, Raney nickel and bare NF are 81.4 mF cm^{-2}, 2.7 mF cm^{-2},45.4 mF cm^{-2} and 2.1 mF cm^{-2}, respectively. The FeCoNiAlMo catalyst exhibited the largest ECSA, which demonstrated its potential for enhancing the water splitting activity. EIS measurements were conducted to evaluate the electron transport ability of the MPEA catalyst. As shown in the Nyquist plots (Fig. 5e), the FeCoNiAlMo catalyst displayed the smallest diameter of the characteristic semicircle, indicating improved electron transfer ability, which could enhance the electrocatalytic kinetics [64]. Chronoamperometry tests were employed to evaluate the stability of the FeCoNiAlMo catalyst. As shown in Fig. 5f for the HER stability test, only slight declines of 30 mV were found after testing for 500 h at current densities of 100 mA cm^{-2}.

In order to comprehensively understand the enhanced water dissociation ability on the FeCoNiAlMo catalyst, operando Raman spectroscopy was conducted at various potential. As depicted in Fig. 5g and h, one broad peak at the Raman shift of around 3500 cm^{-1} can be observed in the spectra, which can be ascribed to the water at the catalyst-electrolyte interface. Furthermore, this interfacial water peak can be further fitted into three peaks, the features at 3240 and 3440 cm^{-1} correspond to the interfacial adsorbed water molecules that participate in the HER, and the one at 3625 cm^{-1} to the dangling O-H bond of the interfacial water molecule that is inactive toward HER [65]. The intensities of the FeCoNiAl catalyst Raman peaks between 3200 and 3500 cm^{-1} were no significant change as the potential increased to - 120 mV (vs. RHE). However, the intensities of the FeCoNiAlMo catalyst Raman peaks gradually decreased. This suggests that the water dissociation efficiency on the surface of the FeCoNiAlMo catalyst increased with potential [66], which is generally regarded as the rate determining step of the alkaline HER. The corresponding Raman contour map more intuitively reflects the changes in the interfacial water peaks in Fig. 5i.

The state characterization of the electrode after the stability test is an important indicator for verifying the catalytic performance. We analyzed the electrode surface state and electrolyte composition after the stability test. The XRD pattern of the FeCoNiAlMo electrode after the stability test in Fig. S7 shows that the electrode still maintains the original B2 structure. This means no significant phase separation or segregation in the alloy crystal structure. After the long-term durability test, The XPS profiles of the used powder indicated that the zero-valent metallic elements transformed to higher valence states (Fig. S8), revealing the contribution of chemical synergetic effect to the excellent electrocatalytic performance. After the long-term stability test for 500 h, the SEM-EDS results (Fig. S9) indicated that the distribution of elements on the used powder surface was still uniform. However, the stability test resulted in the formation of micropores and wrinkles on the used powder, mainly caused by surface oxidation and minor metal dissolution. We performed the ICP-OES test on the element content in the electrolyte after electrolysis to determine the amount of dissolved metal (after the stability test at 100 mA cm^{-2} for 500 h). The results (Table S5) show that the dissolved amount of Al is high (7.81 ppm). This is mainly because Al is difficult to exist stably in an alkaline environment, where the long-term anodic polarization and KOH corrosion lead to the dissolution of Al. However, the dissolved amount of Fe, Co, Ni, and Mo is low (0.44 ppm for Fe, 0.06 ppm for Co, 0.05 ppm for Ni, and 1.31 ppm for Mo). This result directly proves the excellent electrocatalytic stability of the used powder.

3.3. Mechanistic insights

A triple-phase hybrid alloy was deliberately designed and synthesized as a precursor, which leveraged the distinct thermodynamic stability and electrochemical dissolution behavior of each phase in an alkaline electrolyte. This design enabled the selective and complete etching of the FCC and tetragonal phases, while the primary BCC phase transformed into the B2 structure to serve as a structural skeleton and conductive skeleton, which provided efficient electron transport pathways throughout the electrocatalyst [67,68]. The FCC phase, which contained multiple transition metals such as Ni, Fe, and Co, acted as a supply source for active elements. During etching, this phase was preferentially dissolved, releasing metal ions that subsequently underwent hydrolysis, oxidation, and redeposition near the electrode surface. This process led to the in-situ formation of nanocrystalline metal oxides that functioned as highly active sites for the alkaline HER.

Simultaneously, the tetragonal phase, which was rich in Al and Mo, served as a source for metallic glass phase formation. The rapid selective dissolution of Al resulted in the abrupt enrichment of Mo at the solid-liquid interface. As a potent amorphous-forming element, Mo impeded atomic rearrangement and crystallization, thereby facilitating the formation of a Mo-rich glass phase. This metallic glass phase encapsulated the nanocrystals, which not only enhanced the structural stability by preventing nanoparticle agglomeration but also exposed numerous defective sites due to its long-range disordered structure, thereby facilitating the adsorption and desorption of water molecules [69,70]. Moreover, the interfaces between the metallic glass phase and the nanocrystals promoted rapid charge transfer significantly enhancing the intrinsic catalytic activity [71,72]. Through this precisely controlled dealloying process, each of the three phases fulfilled its designated function, collectively contributing to the high activity and stability of the resulting HER electrocatalyst.

4. Discussions

This study validates that combining rational multiphase precursor design with controlled dealloying is a potent strategy for constructing MPEA catalysts with superior activity and robust stability. The essence of this strategy lies in leveraging the distinct thermodynamic and electrochemical stabilities of constituent phases to direct the material's evolution during corrosion, ultimately forming a unique nanocrystalline-glass composite structure rich in heterogeneous interfaces. This tailored microstructure not only provides a high density of active sites but also optimizes reaction pathways and electron transfer through synergistic effects between the phases, collectively contributing to the exceptional HER performance in alkaline electrolyte, notably an ultra-low overpotential of 35 mV at 10 mA cm^{-2} and outstanding long-term durability enduring 500 h of operation at 100 mA cm^{-2}. More importantly, this work moves beyond conventional element-screening approaches by demonstrating how “phase engineering” at the microstructural level can effectively tailor the local atomic environment, thereby opening new avenues for the rational design of next-generation, high-performance, and compositionally complex catalytic material systems.

CRediT authorship contribution statement

Huahai Chang: Writing – review & editing, Writing – original draft, Visualization, Validation, Methodology, Investigation, Formal analysis, Data curation, Conceptualization. **Yiyuan Yang:** Writing – review & editing, Formal analysis, Data curation. **Fan Yu:** Formal analysis. **Shunda Jiang:** Formal analysis. **Xueqian Wang:** Formal analysis. **Zhe Jia:** Writing – review & editing, Visualization, Validation, Supervision, Resources, Project administration, Methodology, Funding acquisition, Formal analysis, Conceptualization. **Baolong Shen:** Writing – review & editing, Visualization, Validation, Supervision, Resources, Project administration, Funding acquisition, Formal analysis, Conceptualization.

Declaration of competing interest

The authors declare the following financial interests/personal

relationships which may be considered as potential competing interests.

Acknowledgements

We acknowledge the financial support by the National Natural Science Foundation of China (52231005, 52571182, 52201174), Natural Science Foundation of Jiangsu Province (BK20253026, BK20220858).

Appendix A. Supplementary data

Supplementary data to this article can be found online at https://doi.org/10.1016/j.pnsc.2025.12.001.

References

[1] N. Johnson, M. Liebreich, D.M. Kammen, P. Ekins, R. McKenna, I. Staffell, Realistic roles for hydrogen in the future energy transition, Nat. Rev. Clean Technol. 1 (2025) 351–371, https://doi.org/10.1038/s44359-025-00050-4.
[2] X. Yang, C.P. Nielsen, S. Song, M.B. McElroy, Breaking the hard-to-abate bottleneck in China's path to carbon neutrality with clean hydrogen, Nat. Energy 7 (2022) 955–965, https://doi.org/10.1038/s41560-022-01114-6.
[3] M.F. Lagadec, A. Grimaud, Water electrolysers with closed and open electrochemical systems, Nat. Mater. 19 (2020) 1140–1150, https://doi.org/10.1038/s41563-020-0788-3.
[4] J.-T. Ren, L. Chen, H.-Y. Wang, W.-W. Tian, Z.-Y. Yuan, Water electrolysis for hydrogen production: from hybrid systems to self-powered/catalyzed devices, Energy Environ. Sci. 17 (2024) 49–113, https://doi.org/10.1039/d3ee02467a.
[5] J. Masa, C. Andronescu, W. Schuhmann, Electrocatalysis as the nexus for sustainable renewable energy: the gordian knot of activity, stability, and selectivity, Angew. Chem. Int. Ed. Engl. 59 (2020) 15298–15312, https://doi.org/10.1002/anie.202007672.
[6] R. Wan, T. Yuan, L. Wang, B. Li, M. Liu, B. Zhao, Earth-Abundant electrocatalysts for acidic oxygen evolution, Nat. Catal. 7 (2024) 1288–1304, https://doi.org/10.1038/s41929-024-01266-6.
[7] T. Kuang, L. Deng, M. Liu, Y. Ding, W. Guo, Z. Cai, W. Liu, Z.X. Huang, Facet engineering of metal-organic frameworks for triboelectric nanogenerators-based self-powered water splitting, Adv. Mater. 37 (2025) e2415616, https://doi.org/10.1002/adma.202415616.
[8] D. Li, M. Chen, D. Liu, C. Shen, H. Sun, Y. Zhang, T. He, Q. Lu, B. Li, T. Zhou, B. Wang, Y. Wu, G. Na, Y. Chen, J. Zhao, Y. Zhang, J. Zhang, F. Liu, H. Cui, Q. Liu, Engineering ruthenium species on metal–organic frameworks for water electrolysis at industrial current densities, Adv. Energy Mater. 15 (2024) 2404714, https://doi.org/10.1002/aenm.202404714.
[9] N. Sun, S.S.A. Shah, Z. Lin, Y.Z. Zheng, L. Jiao, H.L. Jiang, MOF-based electrocatalysts: an overview from the perspective of structural design, Chem Rev 125 (2025) 2703–2792, https://doi.org/10.1021/acs.chemrev.4c00664.
[10] C. Jia, Q. Sun, R. Liu, G. Mao, T. Maschmeyer, J.J. Gooding, T. Zhang, L. Dai, C. Zhao, Challenges and opportunities for single-atom electrocatalysts: from lab-scale research to potential industry-level applications, Adv. Mater. 36 (2024) 2404659, https://doi.org/10.1002/adma.202404659.
[11] G. Zhong, R. Zhao, Y.-R. Shi, C.-R. Li, L. He, L. He, Y. Huang, Thermal shock synthesis of carbon nanotubes supporting small-sized rhenium nanoparticles for efficient electrocatalytic hydrogen evolution, Rare Met. 42 (2023) 2166–2173, https://doi.org/10.1007/s12598-022-02259-9.
[12] S. Shen, Q. Li, H. Zhang, D. Yang, J. Gong, L. Gu, T. Gao, W. Zhong, Negative-Valent platinum stabilized by pt horizontal line Ni electron bridges on oxygen-deficient NiFe-LDH for enhanced electrocatalytic hydrogen evolution, Adv. Mater. 37 (2025) e2500595, https://doi.org/10.1002/adma.202500595.
[13] Y. Tang, Q. Liu, L. Dong, H.B. Wu, X.-Y. Yu, Activating the hydrogen evolution and overall water splitting performance of NiFe LDH by cation doping and plasma reduction, Appl. Catal., B 266 (2020) 118627, https://doi.org/10.1016/j.apcatb.2020.118627.
[14] Z. Jia, Y. Zhao, Q. Wang, F. Lyu, X. Tian, S.-X. Liang, L.-C. Zhang, J. Luan, Q. Wang, L. Sun, T. Yang, B. Shen, Nanoscale heterogeneities of non-noble iron-based metallic glasses toward efficient water oxidation at industrial-level current densities, ACS Appl. Mater. Interfaces 14 (2022) 10288–10297, https://doi.org/10.1021/acsami.1c22294.
[15] R.-Q. Li, H. Su, S.-X. Xie, X.-Y. Wan, C.-M. Wang, G.-Y. Zhang, M.-Z. Ge, J.-M. Dai, C.-Z. Xue, C.-R. Li, J. Cao, W. Zhang, Constructing Fe-Co_2P/CeO_2 heterostructure nanosheet arrays for attaining energy-saving hydrogen production in seawater, Rare Met. 43 (2024) 6426–6435, https://doi.org/10.1007/s12598-024-02932-1.
[16] S. Jiang, G. Cao, Z. Jia, L. Sun, C. Wang, H. Fan, Y. Wang, W. Xu, Y. Cui, Z. Ning, J. Sun, J. Li, X. Tang, H. Liang, E. Peng, A superb iron-based glassy-crystal alloy fiber as an ultrafast and stable catalyst for advanced oxidation, Adv. Fiber Mater. 6 (2024) 1483–1494, https://doi.org/10.1007/s42765-024-00426-4.
[17] S. Gong, Y. Meng, Z. Jin, H.-Y. Hsu, M. Du, F. Liu, Recent progress on the stability of electrocatalysts under high current densities toward industrial water splitting, ACS Catal. 14 (2024) 14399–14435, https://doi.org/10.1021/acscatal.4c03700.
[18] Y.M. Chen, Y.H. Xiao, G.-J. Lyu, B. Wang, Y.-J. Wang, Y. Yang, E. Pineda, C. Fusco, L. Chazeau, J.C. Qiao, Dynamic relaxation in metallic glasses: a unified view from quasi-point defects and fractional viscoelasticity, Int. J. Eng. Sci. 217 (2025) 104394, https://doi.org/10.1016/j.ijengsci.2025.104394.
[19] J.B. Cui, G.H. Xing, G.-J. Lyu, Y.-J. Wang, T. Wada, H. Kato, V.A. Khonik, Y. Yang, J.C. Qiao, Unveiling creep mechanisms in metallic glasses via fractional modeling under coupled thermo-mechanical loads, Int. J. Plast. 195 (2025) 104511, https://doi.org/10.1016/j.ijplas.2025.104511.
[20] Y. Yang, Z. Jia, Q. Wang, Y. Liu, L. Sun, B. Sun, J. Kuang, S. Dai, J. He, S. Liu, L. Duan, H. Tang, L.-C. Zhang, J.J. Kruzic, J. Lu, B. Shen, Vacancy induced microstrain in high-entropy alloy film for sustainable hydrogen production under universal pH conditions, Energy Environ. Sci. 17 (2024) 5854–5865, https://doi.org/10.1039/d4ee01139b.
[21] Y. Yang, Z. Jia, X. Zhang, Y. Liu, Q. Wang, Y. Li, L. Shao, S. Di, J. Kuang, L. Sun, L.-C. Zhang, J.J. Kruzic, Y. Lu, J. Lu, B. Shen, Chemical short-range order in multi-principal element alloy with ordering effects on water electrolysis performance, Mater. Today 72 (2024) 97–108, https://doi.org/10.1016/j.mattod.2023.12.006.
[22] W.-T. Zhang, X.-Q. Wang, F.-Q. Zhang, X.-Y. Cui, B.-B. Fan, J.-M. Guo, Z.-M. Guo, R. Huang, W. Huang, X.-B. Li, M.-R. Li, Y. Ma, Z.-H. Shen, Y.-G. Sun, D.-Z. Wang, F.-Y. Wang, L.-Q. Wang, N. Wang, T.-L. Wang, W. Wang, X.-Y. Wang, Y.-H. Wang, F.-J. Yu, Y.-Z. Yin, L.-K. Zhang, Y. Zhang, J.-Y. Zhang, Q. Zhao, Y.-P. Zhao, X.-D. Zhu, Y. Sohail, Y.-N. Chen, T. Feng, Q.-L. Gao, H.-Y. He, Y.-J. Huang, Z.-B. Jiao, H. Ji, Y. Jiang, Q. Li, X.-M. Li, W.-B. Liao, H.-J. Lin, H. Liu, Q. Liu, Q.-F. Liu, W.-D. Liu, X.-J. Liu, Y. Lu, Y.-P. Lu, W. Ma, X.-F. Miao, J. Pan, Q. Wang, H.-H. Wu, Y. Wu, T. Yang, W.-M. Yang, Q. Yu, J.-Y. Zhang, Z.-G. Chen, L. Mao, Y. Ren, B.-L. Shen, X.-L. Wang, Z. Jia, H. Zhu, Z.-D. Wu, S. Lan, Frontiers in high entropy alloys and high entropy functional materials, Rare Met. 43 (2024) 4639–4776, https://doi.org/10.1007/s12598-024-02852-0.
[23] C. Lin, Q. Wang, H. Liu, Y. Rao, J. Cui, H. Liu, J. Chen, W. Shi, L. Zhang, B. Song, Y. Yao, Direct laser writing of bioinspired high-entropy oxide nanoarrays for practical water electrolysis, Adv. Energy Mater. (2025) e03929, https://doi.org/10.1002/aenm.202503929.
[24] T. Zhang, Q. Liu, H. Bao, M. Wang, N. Wang, B. Zhang, H.J. Fan, Atomically thin high-entropy oxides via naked metal ion self-assembly for proton exchange membrane electrolysis, Nat. Commun. 16 (2025) 1037, https://doi.org/10.1038/s41467-025-56189-y.
[25] H. Cai, S. He, H. Yang, Q. Huang, F. Luo, Q. Hu, X. Zhang, C. He, Highly exposed ultra-small high-entropy sulfides with d-p orbital hybridization for efficient oxygen evolution, Adv. Mater. 37 (2025) e2508610, https://doi.org/10.1002/adma.202508610.
[26] X. Li, Z. Xie, S. Roy, L. Gao, J. Liu, B. Zhao, R. Wei, B. Tang, H. Wang, P. Ajayan, K. Tang, Amorphous high-entropy phosphide nanosheets with multi-atom catalytic sites for efficient oxygen evolution, Adv. Mater. 37 (2025) e2410295, https://doi.org/10.1002/adma.202410295.
[27] Z. Jia, T. Yang, L. Sun, Y. Zhao, W. Li, J. Luan, F. Lyu, L.C. Zhang, J.J. Kruzic, J. J. Kai, J.C. Huang, J. Lu, C.T. Liu, A novel multinary intermetallic as an active electrocatalyst for hydrogen evolution, Adv. Mater. 32 (2020) e2000385, https://doi.org/10.1002/adma.202000385.
[28] X. Gao, W. Lu, S. Shuang, Q. He, Z. Ding, Y. Liu, B. Guo, Z. Jia, S. Zhao, Y. Yang, In situ formation of multi-principal element oxide on a bulk nanoporous intermetallic alloy for ultra-efficient hydrogen production at ampere-level current density, ACS Appl. Mater. Interfaces 17 (2025) 32392–32399, https://doi.org/10.1021/acsami.5c03821.
[29] Z. Jia, K. Nomoto, Q. Wang, C. Kong, L. Sun, L.C. Zhang, S.X. Liang, J. Lu, J. J. Kruzic, A self-supported high-entropy metallic glass with a nanosponge architecture for efficient hydrogen evolution under alkaline and acidic conditions, Adv. Funct. Mater. 31 (2021) 2101586, https://doi.org/10.1002/adfm.202101586.
[30] X. Zhang, Y. Yang, Y. Liu, Z. Jia, Q. Wang, L. Sun, L.C. Zhang, J.J. Kruzic, J. Lu, B. Shen, Defect engineering of a high-entropy metallic glass surface for high-performance overall water splitting at ampere-level current densities, Adv. Mater. 35 (2023) e2303439, https://doi.org/10.1002/adma.202303439.
[31] Z. Jia, Y. Yang, Q. Wang, C. Kong, Y. Yao, Q. Wang, L. Sun, B. Shen, J.J. Kruzic, An ultrafast and stable high-entropy metallic glass electrode for alkaline hydrogen evolution reaction, ACS Mater. Lett. 4 (2022) 1389–1396, https://doi.org/10.1021/acsmaterialslett.2c00371.
[32] Z.W. Chen, J. Li, P. Ou, J.E. Huang, Z. Wen, L. Chen, X. Yao, G. Cai, C.C. Yang, C. V. Singh, Q. Jiang, Unusual sabatier principle on high entropy alloy catalysts for hydrogen evolution reactions, Nat. Commun. 15 (2024) 359, https://doi.org/10.1038/s41467-023-44261-4.
[33] L. Xiao, Z. Wang, J. Guan, Optimization strategies of high-entropy alloys for electrocatalytic applications, Chem. Sci. 14 (2023) 12850–12868, https://doi.org/10.1039/d3sc04962k.
[34] H. Zhu, S. Sun, J. Hao, Z. Zhuang, S. Zhang, T. Wang, Q. Kang, S. Lu, X. Wang, F. Lai, T. Liu, G. Gao, M. Du, D. Wang, A high-entropy atomic environment converts inactive to active sites for electrocatalysis, Energy Environ. Sci. 16 (2023) 619–628, https://doi.org/10.1039/d2ee03185j.
[35] G. Liu, C. Song, X. Li, Q. Jia, P. Wu, Z. Lou, Y. Ma, X. Cui, X. Zhou, L. Jiang, Defect-rich FeCoNiMnRu high-entropy alloys with activated interfacial water for boosting alkaline water/seawater hydrogen evolution, Chem. Eng. J. 509 (2025) 161070, https://doi.org/10.1016/j.cej.2025.161070.
[36] Z. Lu, W. Sun, P. Cai, L. Fan, K. Chen, J. Gao, H. Zhang, J. Chen, Z. Wen, High-entropy alloy catalysts for advanced hydrogen-production zinc-based batteries, Energy Environ. Sci. 18 (2025) 2918–2930, https://doi.org/10.1039/d4ee05500d.
[37] Q. Wang, Y. Qin, J. Xie, Y. Kong, Q. Sun, Z. Wei, S. Zhao, Size-Controllable high-entropy alloys toward stable hydrogen production at industrial-scale current densities, Adv. Mater. 37 (2025) e2420173, https://doi.org/10.1002/adma.202420173.
[38] Y. Li, Z. Dou, Y. Pan, H. Zhao, L. Yao, Q. Wang, C. Zhang, Z. Yue, Z. Zou, Q. Cheng, H. Yang, Crystalline phase engineering to modulate the interfacial interaction of

the ruthenium/molybdenum carbide for acidic hydrogen evolution, Nano Lett. 24 (2024) 5705–5713, https://doi.org/10.1021/acs.nanolett.4c00495.
[39] J. Li, M. Yao, Z. Yuan, J. Ma, S. Geng, F. Liu, Phase engineering boosting heterogeneous interface effect in RuO_2/MnO_2 catalysts for acidic oxygen evolution reaction, Chem. Eng. J. 496 (2024) 153921, https://doi.org/10.1016/j.cej.2024.153921.
[40] Z. Tao, H. Zhao, N. Lv, X. Luo, J. Yu, X. Tan, S. Mu, Crystalline/amorphous-Ru/VO_x phase engineering expedites the alkaline hydrogen evolution kinetics, Adv. Funct. Mater. 34 (2024) 2312987, https://doi.org/10.1002/adfm.202312987.
[41] S. Sun, Z. Wan, Y. Xu, X. Zhou, W. Gao, J. Qian, J. Gao, D. Cai, Y. Ge, H. Nie, Z. Yang, Phase engineering modulates the electronic structure of the IrO_2/MoS_2 heterojunction for efficient and stable water splitting, ACS Nano 19 (2025) 12090–12101, https://doi.org/10.1021/acsnano.4c18288.
[42] J. Gu, F. Duan, S. Liu, W. Cha, J. Lu, Phase engineering of nanostructural metallic materials: classification, structures, and applications, Chem Rev 124 (2024) 1247–1287, https://doi.org/10.1021/acs.chemrev.3c00514.
[43] S. Geng, Y. Ji, J. Su, Z. Hu, M. Fang, D. Wang, S. Liu, L. Li, Y. Li, J.M. Chen, J.F. Lee, X. Huang, Q. Shao, Homogeneous metastable hexagonal phase iridium enhances hydrogen evolution catalysis, Adv Sci 10 (2023) e2206063, https://doi.org/10.1002/advs.202206063.
[44] Z.X. Qian, G.H. Liang, L.F. Shen, G. Zhang, S. Zheng, J.H. Tian, J.F. Li, H. Zhang, Phase engineering facilitates O-O coupling via lattice oxygen mechanism for enhanced oxygen evolution on nickel-iron phosphide, J. Am. Chem. Soc. 147 (2025) 1334–1343, https://doi.org/10.1021/jacs.4c15847.
[45] H. Yang, N. An, Z. Kang, P.W. Menezes, Z. Chen, Understanding advanced transition metal-based two electron oxygen reduction electrocatalysts from the perspective of phase engineering, Adv. Mater. 36 (2024) e2400140, https://doi.org/10.1002/adma.202400140.
[46] H. Shen, H. Jin, H. Li, H. Wang, J. Duan, Y. Jiao, S.Z. Qiao, Acidic CO_2-to-HCOOH electrolysis with industrial-level current on phase engineered tin sulfide, Nat. Commun. 14 (2023) 2843, https://doi.org/10.1038/s41467-023-38497-3.
[47] X. Zhu, Y.C. Wang, K. Qu, L. Song, J. Wang, Y. Gong, X. Liu, C.F. Li, S. Yuan, Q. Lu, A.L. Wang, Modulating Ru-Co bond lengths in Ru_1Co single-atom alloys through crystal phase engineering for electrocatalytic nitrate-to-ammonia conversion, Nat. Commun. 16 (2025) 5742, https://doi.org/10.1038/s41467-025-61232-z.
[48] R. Zhang, Y. Zhang, B. Xiao, S. Zhang, Y. Wang, H. Cui, C. Li, Y. Hou, Y. Guo, T. Yang, J. Fan, C. Zhi, Phase engineering of high-entropy alloy for enhanced electrocatalytic nitrate reduction to ammonia, Angew. Chem. Int. Ed. Engl. 63 (2024) e202407589, https://doi.org/10.1002/anie.202407589.
[49] L. Zheng, Y. Zhang, W. Chen, X. Xu, R. Zhang, X. Ren, X. Liu, W. Wang, J. Qi, G. Wang, C. Ma, L. Xu, P. Han, Q. He, D. Ma, J. Wang, C. Ling, D. Su, M. Shao, Y. Chen, Carbon-eextraction-triggered phase engineering of rhodium nanomaterials for efficient electrocatalytic nitrate reduction reaction, Angew. Chem. Int. Ed. Engl. 64 (2025) e202500985, https://doi.org/10.1002/anie.202500985.
[50] M. Wang, W. Zhang, F. Zhang, Z. Zhang, B. Tang, J. Li, X. Wang, Theoretical expectation and experimental implementation of in situ Al-doped CoS_2 nanowires on dealloying-derived nanoporous intermetallic substrate as an efficient electrocatalyst for boosting hydrogen production, ACS Catal. 9 (2019) 1489–1502, https://doi.org/10.1021/acscatal.8b04502.
[51] Y. Kang, C. Zhang, H. Li, Y. Li, H. Lei, R. Huang, Y. Han, W. Wei, X. Zhao, Y. Cui, Tailoring OH formation and desorption on nickel catalysts via surface oxidation for enhanced hydrogen evolution stability and kinetics, ACS Catal. 15 (2025) 8768–8775, https://doi.org/10.1021/acscatal.4c07829.
[52] Y. Zhao, L. Li, Z. Wang, W. Li, Z. Han, Y. Cui, Z. Duan, W. Wang, X. Fu, Synergistic Fe/Co doping and vacancy engineering for stable RuO_x in acidic OER, ACS Appl. Mater. Interfaces 17 (2025) 49461–49471, https://doi.org/10.1021/acsami.5c09976.
[53] Y. Cheng, T. Zhai, X. Yong, R. Zhang, D. Pan, Y. Yuan, Z. Tang, H. Wang, S. Lu, Grain-boundary-rich Mo-doped RuO_2 for highly efficient and stable proton-exchange-membrane water electrolysis, ACS Nano 19 (2025) 34329–34340, https://doi.org/10.1021/acsnano.5c12133.
[54] L. Zhang, D. Zhou, B. Li, Anomalous microstructure and excellent mechanical properties of $Ni_{35}Al_{21.67}Cr_{21.67}Fe_{21.67}$ high-entropy alloy with BCC and B2 structure, Mater. Lett. 216 (2018) 252–255, https://doi.org/10.1016/j.matlet.2018.01.124.
[55] Z. Zhu, Y. Bai, T. Zhang, Z. Liu, X. Long, Z. Wei, Z. Wang, L. Zhang, J. Wang, F. Yan, S. Yang, High-performance hole-extraction layer of sol–gel-processed NiO nanocrystals for inverted planar perovskite solar cells, Angew. Chem. Int. Ed. 53 (2014) 12571–12575, https://doi.org/10.1002/anie.201405176.
[56] Q. Wang, Z. Jia, J. Li, Y. He, Y. Yang, Y. Li, L. Sun, B. Shen, Attractive electron delocalization behavior of FeCoMoPB amorphous nanoplates for highly efficient alkaline water oxidation, Small 18 (2022) 2204135, https://doi.org/10.1002/smll.202204135.
[57] X. Zhang, X. Li, Z. Pan, Y. Lai, Y. Lu, Y. Wang, S. Song, Boosting hydrogen evolution electrocatalysis through defect engineering: a strategy of heat and cool shock, Chem. Eng. J. 426 (2021) 131524, https://doi.org/10.1016/j.cej.2021.131524.
[58] D.D. Alemayehu, M.-C. Tsai, M.-H. Tsai, C.-C. Yang, C.-C. Chang, C.-Y. Chang, E. A. Moges, K. Lakshmanan, Y. Nikodimos, W.-N. Su, C.-H. Wang, B.J. Hwang, Heterogeneous interfaces of Ni_3Se_4 nanoclusters decorated on a Ni_3N surface enhance efficient and durable hydrogen evolution reactions in alkaline electrolyte, J. Am. Chem. Soc. 147 (2025) 16047–16059, https://doi.org/10.1021/jacs.4c17747.
[59] H. Zhao, S. Zhu, Z. Cui, Z. Li, S. Wu, W. Xu, Z. Gao, Y. Liang, L. Ma, H. Jiang, Toward scalable synthesis of $Mo_2C/MoNi_4$ heterojunction catalysts on Ni mesh via laser radiation for efficient H_2 production in alkaline electrolysis, Adv. Funct. Mater. 35 (2025) 2423549, https://doi.org/10.1002/adfm.202423549.
[60] Y. He, J. Qin, F. Hu, L. Mao, B. Shen, T.M. Aminabhavi, Y. Vasseghian, A. Hojjati-Najafabadi, Chemical dealloying derived nanoporous FeCoNiCuTi high-entropy bifunctional electrocatalysts for highly efficient overall water splitting under alkaline conditions, Chem. Eng. J. 492 (2024) 152145, https://doi.org/10.1016/j.cej.2024.152145.
[61] R. Li, X. Liu, W. Liu, Z. Li, K.C. Chan, Z. Lu, Design of hierarchical porosity via manipulating chemical and microstructural complexities in high-entropy alloys for efficient water electrolysis, Adv. Sci. 9 (2022) 2105808, https://doi.org/10.1002/advs.202105808.
[62] X. Yu, J. Zhao, M. Johnsson, Interfacial engineering of nickel hydroxide on cobalt phosphide for alkaline water electrocatalysis, Adv. Funct. Mater. 31 (2021) 2101578, https://doi.org/10.1002/adfm.202101578.
[63] Y. Long, G. Zhao, L. Yang, Y. Xu, C. Xu, Carbon dot embedded CoNi bimetallic phosphide nanorods as an efficient electrocatalyst for overall water splitting, J. Mater. Chem. A. 12 (2024) 33301–33313, https://doi.org/10.1039/d4ta04340e.
[64] Y.P. Wu, W. Zhou, J. Zhao, W.W. Dong, Y.Q. Lan, D.S. Li, C. Sun, X. Bu, Surfactant-assisted phase-selective synthesis of new cobalt MOFs and their efficient electrocatalytic hydrogen evolution reaction, Angew. Chem. Int. Ed. 56 (2017) 13001–13005, https://doi.org/10.1002/anie.201707238.
[65] Q. Dai, L. Wang, K. Wang, X. Sang, Z. Li, B. Yang, J. Chen, L. Lei, L. Dai, Y. Hou, Accelerated water dissociation kinetics by electron-enriched cobalt sites for efficient alkaline hydrogen evolution, Adv. Funct. Mater. 32 (2021) 2109556, https://doi.org/10.1002/adfm.202109556.
[66] K. Wang, J. Cao, X. Yang, X. Sang, S. Yao, R. Xiang, B. Yang, Z. Li, T. O'Carroll, Q. Zhang, L. Lei, G. Wu, Y. Hou, Kinetically accelerating elementary steps via bridged Ru-H state for the hydrogen-evolution in anion-exchange membrane electrolyzer, Adv. Funct. Mater. 33 (2023) 2212321, https://doi.org/10.1002/adfm.202212321.
[67] S.R. Butler, J.E. Hanlon, R.J. Wasilewski, Electric and magnetic properties of B2 structure compounds: nial, CoAl, J. Phys. Chem. Solids. 30 (1969) 1929–1934, https://doi.org/10.1016/0022-3697(69)90168-1.
[68] R.B. Capaz, M. ElMassalami, L.A. Terrazos, M. Elhadi, H. Takeya, L. Ghivelder, Boron-substitution and defects in B2-type AlNi compound: Site-preference and influence on structural, thermodynamic and electronic properties, J. Alloys Compd. 669 (2016) 210–216, https://doi.org/10.1016/j.jallcom.2016.01.244.
[69] B. Zeng, X. Liu, L. Wan, C. Xia, L. Cao, Y. Hu, B. Dong, Grafting ultra-fine nanoalloys with amorphous skin enables highly active and long-lived acidic hydrogen production, Angew. Chem. Int. Ed. 63 (2024) e202400582, https://doi.org/10.1002/anie.202400582.
[70] Y. Wang, X. Li, Z. Huang, H. Wang, Z. Chen, J. Zhang, X. Zheng, Y. Deng, W. Hu, Amorphous Mo-doped $NiS_{0.5}Se_{0.5}$ nanosheets@crystalline $NiS_{0.5}Se_{0.5}$ nanorods for high current-density electrocatalytic water splitting in neutral media, Angew. Chem. Int. Ed. 62 (2023) e202215256, https://doi.org/10.1002/anie.202215256.
[71] J. Ren, Y. Du, Y. Wang, S. Zhao, B. Yang, B. Li, L. Wang, Modulating amorphous/crystalline heterogeneous interface in $RuCoMoyO_x$ grown on nickel foam to achieve efficient overall water splitting, Chem. Eng. J. 469 (2023) 143993, https://doi.org/10.1016/j.cej.2023.143993.
[72] P. Tian, W. Zong, J. Xiong, W. Liu, J. Liu, Y. Dai, J. Zhu, S. Huang, S. Song, K. Chu, G. He, N. Han, Dynamic reconstruction of crystal/amorphous hetero-phosphate janus interfaces for highly stable seawater splitting, Adv. Funct. Mater. 35 (2025) 2504862, https://doi.org/10.1002/adfm.202504862.